Structural and Kinetic Aspects of Bromide Adsorption on Au(100)

Th. Wandlowski*

Department of Electrochemistry, University of Ulm, D-89069 Ulm, Germany

J. X. Wang,[†] O. M. Magnussen,[†] and B. M. Ocko[‡]

Department of Applied Science, Chemical Division, and Department of Physics, Brookhaven National Laboratory, Upton, New York 11973

Received: January 2, 1996; In Final Form: March 27, 1996[⊗]

The adsorption and phase formation of bromide ions on Au(100) has been studied with in-situ surface X-ray diffraction in combination with electrochemical measurements. The investigations allowed a rather detailed assignment of all voltammetric features of the bromide adsorption on Au(100) to the respective structural properties, their stability, and their transition kinetics. The presence of a small bromide surface excess at Au(100)-(hex) causes the lifting of the substrate surface reconstruction. The corresponding charge density just before the onset of the transition ranges from -2 to -8 μC cm^{-2}. No ordering of the adlayer is required or involved. The lifting of the substrate reconstruction proceeds at high overpotentials via instantaneous nucleation and two-dimensional growth. The growth mechanism seems to change at low overpotentials toward a one-dimensional or surface diffusion controlled process. Two ordered bromide adlayer phases were found on the unreconstructed Au(100)-(1×1) surface. The low coverage phase ($\theta = 0.5$) corresponds to a commensurate c($\sqrt{2}$×2$\sqrt{2}$)R45° superstructure. A uniaxial commensurate c($\sqrt{2}$×p)R45° phase is formed at more positive potentials, in which the coverage increases from 0.5 to approximately 0.565 (relative to the gold layer density) with increasing electrode potential. Current vs time measurements revealed that the transition between the disordered fluidlike phase and the commensurate c($\sqrt{2}$×2$\sqrt{2}$)R45° phase proceeds via instantaneous islands (hole) nucleation and activation-controlled growth in combination with a parallel adsorption (desorption) process. The formation of the slightly more dense uniaxial commensurate c($\sqrt{2}$×p)-R45° adlayer can be described with the exponential law of nucleation in combination with either one-dimensional activation-controlled or two-dimensional surface diffusion controlled growth.

1. Introduction

The adsorption of halogen gases on well-defined gold surfaces and of halide anions on the corresponding single crystal electrodes have been studied extensively in the past. In vacuum environment chemisorbed halogens dissociate and form ordered monolayers.[1] These adlayers are often incommensurate with the metal substrate and change continuously with increasing halogen coverage. Equilibrium properties of the superstructures are difficult to obtain in ultrahigh vacuum environment due to the high activation barrier for the adsorption of halogen atoms on gold surfaces. Furthermore, the kinetic mechanisms of adlayer formation are not well identified either.[2] The situation is in some sense less complicated at the Au(*hkl*)/aqueous electrolyte interface, where the chemical potential of the adsorbate can be directly controlled via the applied electrode potential. Cyclic voltammetry and measurements of the differential capacitance vs potential have been applied to qualitatively characterize the interfacial behavior of halide ions on gold single-crystal electrodes.[3−5] The combination of these classical techniques with in-situ, structure-sensitive methods like electroreflectance,[6] second harmonic generation,[7] and surface X-ray scattering (SXS)[8−10] showed unambiguously that the reconstruction of all three low-index gold surfaces is already lifted in the presence of small amounts of specifically adsorbed halide anions. Additional support is available from ex-situ electron diffraction and X-ray photoelectron spectroscopy (XPS) studies

with emersed electrodes.[11−13] The extent of specific halide adsorption on Au(*hkl*) has been quantified employing chronocoulometry[14,15] and measurements with the quartz crystal microbalance.[16] In-situ scanning tunneling microscopy (STM) experiments have demonstrated that the adsorption of even small amounts of halide ions on Au(*hkl*) increases the mobility of gold atoms at steps.[17,18] As a consequence of this anion-enhanced mobility, surface irregularities such as gold clusters and small islands or monatomic holes may disappear rather quickly and the quality of the single-crystal surface improves considerably ("electrochemical annealing"). A comprehensive in-situ STM study of the iodine adsorption on the three low-index faces Au(111), Au(110), and Au(100) illustrates that the anion-induced removal of the substrate reconstruction is followed by the formation of various ordered adlayer phases. The authors also tried to extract information on the phase transition kinetics.[19−21] Structural aspects of the two incommensurate iodine monolayer phases, which are observed on Au(111), have been investigated in remarkable detail using SXS experiments.[22] Much less structural information is known on the lighter halides. Ordered bromide adlayers on Au(111) were found in a preliminary STM study.[23] Recently published X-ray scattering experiments showed convincingly that both bromide and chloride ions form incommensurate, hexagonal close-packed monolayers on Au(111), which compress uniformly with increasing potential.[24]

The present communication is focused on the adsorption and phase behavior of bromide ions on Au(100). The study combines electrochemical measurements with surface X-ray scattering experiments. It will be demonstrated that bromide

---

[†] Department of Applied Science, Chemical Division.
[‡] Department of Physics.
[⊗] Abstract published in *Advance ACS Abstracts,* May 15, 1996.

forms a commensurate c($\sqrt{2} \times 2\sqrt{2}$)R45° adlayer structure on Au(100)-(1×1) which transforms at higher electrode potentials into a uniaxial commensurate c($\sqrt{2} \times p$)R45° phase with $p < 2\sqrt{2}$. We will show, based on these structural data and on the results of potential step experiments, that the kinetics of adlayer formation and dissolution can be described by nucleation- and growth-based models. Dynamic aspects of the stability of the substrate structure will be also discussed in some detail.

2. Experimental Section

The electrochemical measurements were performed in Ulm with Au(100) single-crystal electrodes (4 mm diameter and 4 mm thickness) using the so-called "hanging meniscus" technique.[25] Gold disk electrodes (10 mm diameter, 2 mm thickness) were used in the X-ray measurements. The electrodes were carefully annealed before each experiment and after a short cooling period in air quenched in Milli-Q water. Transfer into the electrochemical or X-ray cell (for details see ref 9) was performed with a protecting droplet of water adhering to the polished surface. Contact with the electrolyte was established under strict potential control. All potentials in subsequent sections are cited with respect to a saturated calomel electrode if not stated otherwise.

The solutions were prepared from Milli-Q water, NaClO$_4$ (Fluka, puriss. p.a.), twice recrystallized, and NaBr (Merck, suprapure). They were deaerated with 5 N nitrogen prior to each experiment. Nitrogen was passed over the electrolyte in the case of the electrochemical measurements or through the outer chamber of the X-ray cell. Most of the experiments were carried out at room temperature, (20 ± 1) °C.

Standard electrochemical equipment was employed for cyclic voltammetry and potential step experiments. Capacitance measurements were performed using a 18 Hz sine wave of 10 mV (peak-to-peak) amplitude superimposed on a voltage ramp or step. Positive feedback was used to compensate the solution resistance. The alternating current was amplified using a lock-in technique (LIA model ITHACO 393), digitized and afterward analyzed with a simple RC equivalent circuit.

The X-ray experiments were carried out with focused monochromatic radiation (λ between 1.2 and 1.77 Å) at the beam lines X22A and X22B of the National Synchrotron Light Source at Brookhaven National Laboratory. The full description of the electrochemical SXS technique has been presented elsewhere.[9] For in-plane diffraction measurements, the Q-space resolution within the scattering plane was primarily determined by the use of a LiF(200) analyzer crystal. This arrangement provides a 2θ resolution of 0.01° half-width at half-maximum (hwhm), which corresponds to a longitudinal in-plane resolution of 0.001 Å^{-1} hwhm. The transverse in-plane resolution was limited by the mosaic spread of the gold crystal, which was about 0.1° hwhm. This is about a factor of 5 smaller than the longitudinal in-plane resolution. In order to describe the scattering wave vector (H,K,L) in terms of its components within the surface plane and along the surface normal, a conventional face-centered (fcc) coordinate system with four gold atoms per unit cell was chosen. The atomic positions can be described by the basis vectors **a**, **b** in plane and by **c** along the surface normal, where $|\mathbf{a}| = |\mathbf{b}| = |\mathbf{c}| = 4.078$ Å = $\sqrt{2}a_{nn}$; $a_{nn} = 2.885$ Å is the gold nearest neighbor separation. The angle between two pairs of vectors is 90°. The corresponding reciprocal space basis is given by ($\mathbf{a^*}, \mathbf{b^*}, \mathbf{c^*}$)($H,K,L$), where $|\mathbf{a^*}| = |\mathbf{b^*}| = |\mathbf{c^*}| = 2\pi/(\sqrt{2}a_{nn})$ = 1.540 Å^{-1}. The in-plane diffraction measurements were carried out in the (H,K) plane with typically $L = 0.1$ corresponding to a grazing incidence angle of 1.1°.
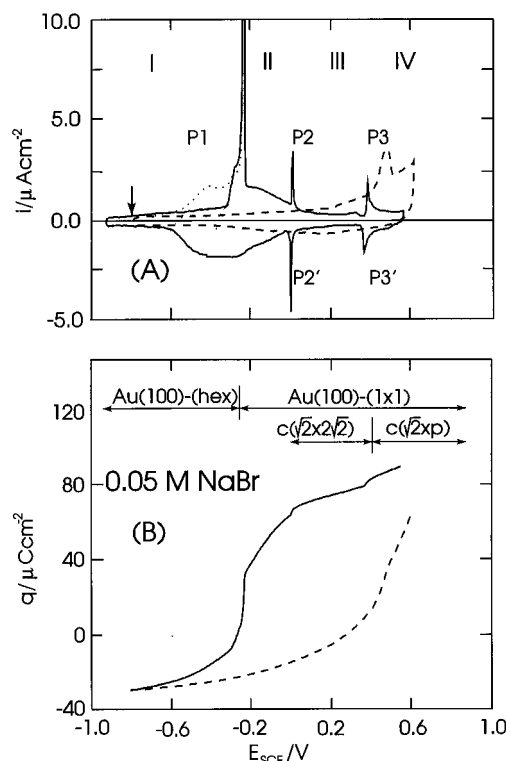

Figure 1. (A) Cyclic voltammogram for Au(100) in 0.05 M NaBr, scan rate 10 mV s^{-1}, temperature 20 °C. The electrode was immersed under potential control at −0.800 V. The first scan is indicated by the solid line; the dotted line represents the second scan. The dashed curve is the first scan for Au(100)/0.05 M NaClO$_4$. The stability of the various substrate surface (Au) and adlayer structures (Br) is also indicated. The transitions are labeled P1, P2/P2′, and P3/P3′, and the stable regions are labeled I, II, III, and IV. (B) Charge density vs potential curves for 0.05 M NaClO$_4$ (---) and 0.05 M NaBr/Au(100) (—) as obtained by integrating the first anodic scan of the voltammogram shown in (A). The independently determined zero charge potential of the 0.05 M NaClO$_4$/Au(100)-(hex) system was chosen as integration constant.

3. Results and Discussion

3.1. Basic Electrochemical Aspects. Figure 1A shows a typical voltammogram for the adsorption of bromide ions on Au(100) in 0.05 M NaBr, at a scan rate of 10 mV s^{-1}. The freshly flame-annealed electrode was brought in contact with the electrolyte solution under potential control at $E = -0.80$ V (indicated by the arrow). This procedure ensures the preservation of the thermally induced reconstructed Au(100)-(hex) surface. The first cycle is symbolized by the thick solid line. The dotted line corresponds to the second cycle, which is practically identical with all subsequent scans. Four different potential regions (I−IV) can be readily distinguished. They are separated by well-defined current peaks labeled P1, P2/P2′, and P3/P3′. The corresponding charge densities, calculated from the first anodic potential scan, amount to 33, 3, and 4 μC cm^{-2}, respectively. Peak P1 is irreversible and cannot be completely recovered after the first cycle. The position is slightly shifted toward more negative potentials, and its height depends significantly on the scan rate and the negative return potential. In analogy to the results of a combined electrochemical and optical study of the adsorption of ClO$_4^-$, SO$_4^{2-}$, and Cl$^-$ ions on Au(100),[6] we may assume that the pronounced current peak P1 signals the lifting of the reconstruction of the gold surface due to bromide adsorption. This hypothesis also implies that region I can be assigned to the reconstructed Au(100)-(hex) surface with minor adsorption of bromide. Regions II−IV should represent the unreconstructed Au(100)-(1×1) phase with varying bromide coverage, which increases with increasing
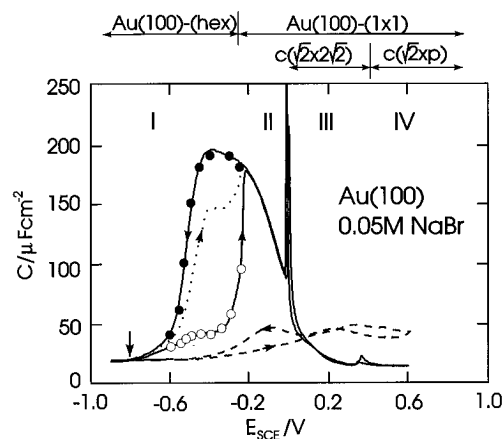
Structural and Kinetic Aspects of Br⁻ Adsorption on Au(100)

J. Phys. Chem., Vol. 100, No. 24, 1996 **10279**

Figure 2. Capacitance vs potential curves for Au(100) in 0.05 M NaBr (—, ⋯) or 0.05 M NaClO₄ (---), scan rate 10 mV s⁻¹, 18 Hz and 10 mV peak-to-peak ac amplitude. The first scan (—) starts at −0.800 V with a freshly flame-annealed electrode. The filled and open circles represent the initial ($t \to 0$) and the final ($t \to \infty$) values of the interfacial capacitance as obtained from single potential step experiments with E_i = −0.100 V and various final values at successively more negative potentials E_f.

potential. The confirmation will be given in section 3.2, based on the results of in-situ surface X-ray diffraction measurements.

The peak pair P2/P2′ is rather sharp and symmetrical. The positional hysteresis between the positive and the negative going scans is less than 20 mV. Morphological similarities to features observed for the adsorption of hydrogen sulfate ions[26] or chloride ions on Au(111)[27] point to a disorder/order phase transition, which involves specifically adsorbed anions. Structural changes within the bromide adlayer may also explain the nature of the most positive pair of peaks, which separates the regions III and IV. It is noteworthy to point out that P3/P3′ shows a few distinct differences in comparison to P2/P2′. The peaks are asymmetric with a round tail toward positive potentials. The hysteresis is more pronounced, too. We also note that neither the regions II−IV nor the peak pairs P2/P2′ and P3/P3′ are sensitive to the number of potential scans or the immersion potential of the electrode. This observation might be related to the anion-enhanced mobility of the gold surface atoms, which causes the formation of island-free Au(100)-(1×1) terraces at potentials positive of −0.20 V.[17,28]

The extent of bromide adsorption was estimated by integrating the current, which corresponds to the positive going sweep in Figure 1A. The charge density vs potential curve is shown in Figure 1B. The data for 0.05 M NaClO₄/Au(100)-(hex) have been added for comparison. The plot was obtained with the separately determined zero charge potential E_{pzc} = 0.276 V of Au(100)-(hex) in 0.05 M NaClO₄ and the assumption that ClO₄⁻ and Br⁻ ions are not adsorbed at $E <$ −0.800 V. This result compares reasonably well with literature data.[6] The charge density curve (Figure 1B) as well as the capacitance vs potential curve (Figure 2) illustrate all four characteristic potential regions, I−IV, and the respective transitions involved in P1, P2/P2′, and P3/P3′ for the adsorption of bromide on Au(100). The capacitance vs potential curve shows under our experimental conditions (18 Hz, 10 mV peak-to-peak ac amplitude, 10 mV s⁻¹) a discontinuity around P1 in the first scan, a sharp needlelike maxima at P2/P2′, and a rather broad feature at P3/P3′. The pronounced hysteresis between the regions I and II, when comparing the first anodic with the first cathodic scan, points to a significant kinetic effect on the reformation of the reconstructed substrate surface after once being lifted. Furthermore, the capacitance of the unreconstructed Au(100)-(1×1)
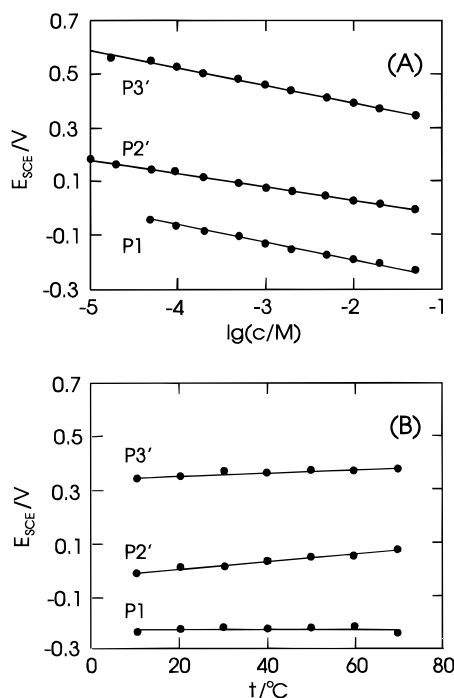

Figure 3. (A) Concentration dependence of the position of the characteristic transition peaks P1, P2′, and P3′ of the system x M NaBr/(0.05 − x) M NaClO₄ as obtained with capacitance or current vs potential measurements similar to those shown in Figure 1 and Figure 2. (B) Temperature dependence of the peaks P1, P2′, and P3′ for 0.05 M NaBr/Au(100) The solid lines indicate the corresponding linear regression fits.

phase seems to be larger than that of the reconstructed Au-(100)-(hex) phase, at constant potential.

We found also that the positions of the transition potentials at P1 (I → II), P2′ (III → II) and P3′ (IV → III) shift with increasing bromide concentration toward negative values for the system (0.05 − x) M NaClO₄/x M NaBr/Au(100). The individual slopes $\delta E/\delta \log c$ were calculated to −62, −50, and −66 mV (Figure 3A). These values point to a rather complete discharge of bromide since the slopes are close to −59 mV, expected on the basis of an electrosorption valency of −1. Because no direct attempt has been made to follow the degree of free bromide charge quantitatively as a function of potential, we will throughout this work use the term bromide in order to avoid confusion (even though it might not always be exact).

Studies of the temperature dependence revealed that the positions of P2/P2′ and P3/P3′ shift toward higher potentials with increasing temperature in 10 °C < t < 70 °C (Figure 3B).

More detailed analysis of the electrochemical adsorption of bromide on Au(100) is severely hampered by the lack of direct structural information. Therefore, we focus in the following sections first on the in-situ X-ray diffraction results. After the discussion of the structure of the gold surface and of the bromide adlayers, we will address kinetic aspects of the phase transitions involved on the basis of current−time measurements.

3.2. In-Situ X-ray Diffraction Studies of Au(100)/0.05 M NaBr. *3.2.1. Stability of the Substrate Surface Structure.* Recent in-situ STM and SXS experiments in 0.1 M H₂SO₄ or 0.1 M HClO₄ have demonstrated that the Au(100) surface exhibits an incommensurate hexagonal reconstruction pattern at sufficiently negative potentials.[8,29−31] There are nearly six surface atoms for every five bulk atoms along the (110) direction. The reconstructed structure can be aligned (thermally reconstructed) or is slightly rotated (electrochemically reconstructed) with respect to the underlying bulk and can be
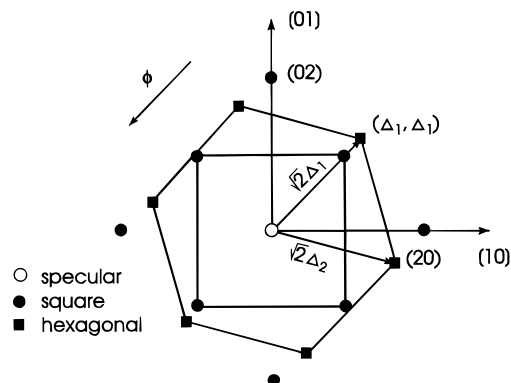
Figure 4. In-plane diffraction pattern of the reconstructed (■) and the unreconstructed (●) Au(100) surface. The characteristic wave vectors Δ_1 and Δ_2 along the [110] and the rotated directions are indicated.[29]
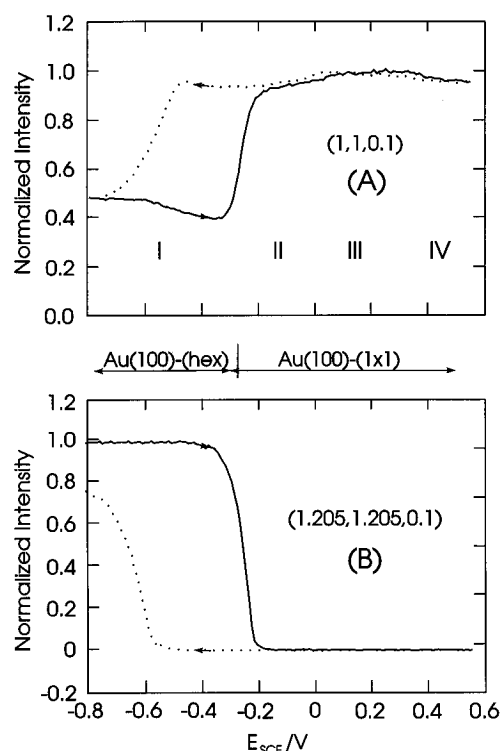

Figure 5. Potential dependencies of the normalized scattering intensity for Au(100) in 0.05 M NaBr at (1,1,0.1) (A) and (1.205,1.205,0.1) (B), which correspond to characteristic reflections of the Au(100)-(1×1) or Au(100)-(hex) surface structure, respectively. Both sets of potential scans (scan rate 10 mV s^{-1}) started with a freshly flame-annealed gold electrode at -0.800 V. The direction of the potential scans is indicated by the arrows.

described by a near-hexagonal pattern centered around the origin. $\Delta_1 = (1.205 \pm 0.002)$ and $\Delta_2 = (1.200 \pm 0.005)$ are the wave vectors along (110) and the rotated directions. The incommensurability is given by $\delta = \Delta_1 - 1 = 0.205$.[29] Here we report similar results in 0.05 M NaBr when measuring the diffraction pattern just after immersion of a freshly tempered Au(100) electrode at $E < -0.400$ V (Figure 4, filled squares). The position of the rocking curve at (1.205,1.205,0.1) is well aligned with the (1,1,0.1) crystal truncation rod of the unreconstructed face.

Following the voltage dependence of the scattering intensity at $(\Delta_1, \Delta_1, 0.1)$ or at (1,1,0.1), it is now possible to monitor the stability of the reconstructed and/or the unreconstructed Au-(100) surface, respectively. The comparison of these data (Figure 5) with the electrochemical measurements (Figure 1 and Figure 2) indicates that region I coincides with the stability range
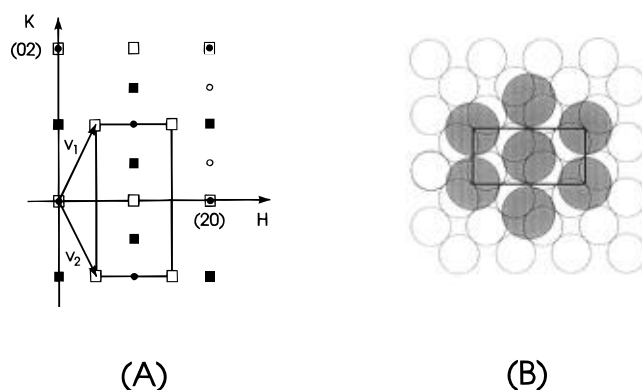

Figure 6. (A) In-plane diffraction pattern of the commensurate c($\sqrt{2}\times2\sqrt{2}$)R45° bromide adlayer structure as obtained at 0.200 V for 0.05 M NaBr/Au(100)-(1×1). The fcc coordinate system was used as reference. The solid circles represent substrate surface reflections. The bromide superstructure reflections are indicated by (□) and (■). The two symbols characterize two different domains, which are rotated by 90° with respect to each other. The basis vectors of the (□) domain, $\mathbf{v}_1$ and $\mathbf{v}_2$, are also shown. The open circles represent experimentally observed weak reflections, which are not expected for the c($\sqrt{2}\times2\sqrt{2}$)R45° structure (cf. ref 33). (B) Real space structure of the c($\sqrt{2}\times2\sqrt{}$)R45° bromide adlayer on Au(100).

of the reconstructed Au(100)-(hex) surface. The sharp peak P1 in the cyclic voltammogram represents the lifting of the reconstruction. The surface forms an ideally terminated Au-(100)-(1×1) phase in regions II, III, and IV. The adlayer structures will be discussed below.

3.2.2. Structure of Bromide Adlayers on Au(100). In regions I and II no diffraction peaks associated with the formation of a well ordered bromide adlayer were observed. Furthermore we note that there is very little change in the (1,1,0.1) intensity in region II. This often indicates the existence of a disordered fluidlike adlayer rather than a lattice gas.[22] Indications for the existence of an ordered bromide adlayer are apparent from the diffraction pattern shown in Figure 6 at more positive potentials, e.g., $E > 0.05$V for $c = 0.05$ M NaBr. In addition to the Au-(100) diffraction features (solid circles), we observe between 0.05 and 0.40 V integer and half-integer reflections (open and filled squares). Further inspection revealed that the diffraction spots symbolized by the squares in Figure 6, can be described by linear combinations of two pairs of base vectors: $\mathbf{v}_1 = 0.5\mathbf{a}^* + \mathbf{b}^*$ and $\mathbf{v}_2 = 0.5\mathbf{a}^* - \mathbf{b}^*$ (□) or $\mathbf{v}_1 = \mathbf{a}^* - 0.5\mathbf{b}^*$ and $\mathbf{v}_2 = \mathbf{a}^* + 0.5\mathbf{b}^*$ (■). This result indicates the existence of two symmetry-equivalent domain structures, which are rotated by 90° with respect to each other. Most of the additional reflections can be attributed to a commensurate bromide adlayer with a centered rectangular unit cell as shown for one domain in Figure 6B. In terms of the gold nearest-neighbor spacing, this cell is referred to as c($\sqrt{2}\times2\sqrt{2}$)R45°, in terms of the fcc coordinates the unit cell is (1 × 2). All of the bromide species are situated in "bridge" sites. The proposed registry between adlayer and substrate surface structure is based on a qualitative intensity analysis and the results of a LEED study on the chemisorption of bromine on Au(100).[32] Weak reflections (open circles in Figure 6A) observed at (2,0.5,0.1) and (2,1.5,0.1), not expected for this commensurate structure, might be artifacts of distortions in the underlying gold layers or in an asymmetric surface Debye−Waller term.[33]

Furthermore, it is important to point out that the commonly observed c(2×2) structure, which also has $\theta = 0.5$ and where the adatoms reside in higher coordinated fourfold hollow sites, does not give rise to the observed diffraction pattern. The symmetry of the c(2×2) phase is square whereas the c($\sqrt{2}\times2\sqrt{2}$)R45° phase is close to hexagonal. The preference

Structural and Kinetic Aspects of Br⁻ Adsorption on Au(100)
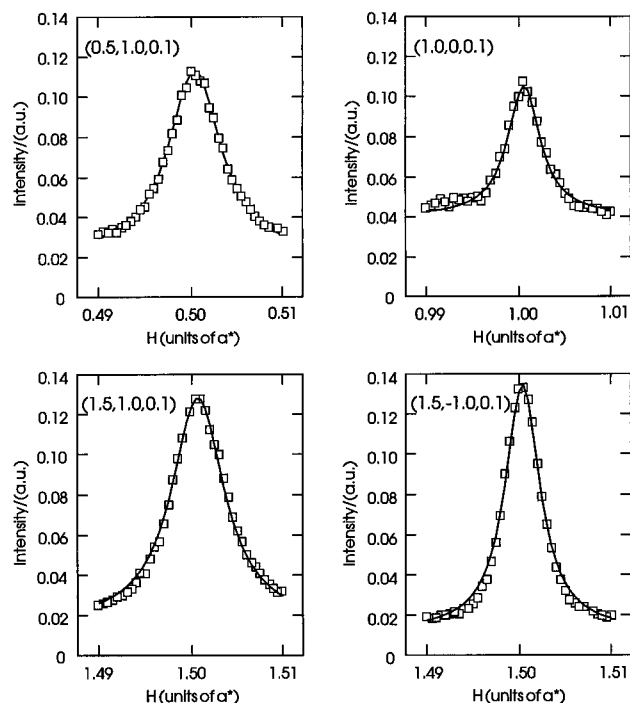
J. Phys. Chem., Vol. 100, No. 24, 1996 **10281**

Figure 7. Typical diffraction profiles of the c($\sqrt{2}\times2\sqrt{2}$)R45° bromide adlayer on Au(100) measured at 0.200 V at different positions in reciprocal space. The solid lines are fits to a Lorenzian line shape.

for the c($\sqrt{2}\times2\sqrt{2}$)R45° suggests that the elastic interactions between the relatively large adsorbate atoms (ions), which favor hexagonal packing, are more significant than the adsorbate–substrate interaction energy difference between the two phases.

It is convenient to define the bromide coverage in units, where unity corresponds to a complete monolayer of Au(100)-(1×1) packed gold surface atoms. The c($\sqrt{2}\times2\sqrt{2}$)R45° unit cell contains two bromide atoms in an area $A_{2Br} = 4a_{nn}^2$, which corresponds to $A_{Br} = 2a_{nn}^2$. The calculated bromide coverage within the entire potential region III amounts to $\theta = A_{Au}/A_{Br} = 0.5$ or 6.03×10^{14} ions cm⁻², where $A_{Au} = a_{nn}^2$ is the area per gold surface atom. This result is in reasonable agreement with 5.43×10^{14} ions cm⁻², which was estimated from the voltammetric data plotted in Figure 1 (at 0.20 V), assuming that the adsorbed "bromide" is neutral.

Figure 7 shows diffraction profiles of the c($\sqrt{2}\times2\sqrt{2}$)R45° bromide adlayer at $E = 0.200$ V and at different positions in reciprocal space. The solid lines are fits to a Lorenzian line shape. The minimum half-width at half-maximum (hwhm) of the superstructure peaks in H and K directions is 0.0022 Å⁻¹. The actual width depends on the potential history.[33] By neglecting the limited resolution and assuming a perfect sample mosaic, we estimate a lower bound of the coherence length (e.g., domain size) of 450 Å, which compares to the size of the Au-(100)-(1×1) facets. Thus the reconstructed Au(100) surface seems to have large terraces in the presence of bromide, which are free of gold islands.

The stability of the c($\sqrt{2}\times2\sqrt{2}$)R45° adlayer structure was monitored by following the potential dependence of the corresponding diffraction profiles at constant positions in reciprocal space. A typical series of so-called diffractograms, which were obtained for the (1,0,0.1) position with scan rates of 1.0 mV s⁻¹ (lines) and 0.2 mV s⁻¹ (circles), is shown in Figure 8. They correspond exactly to the voltammetric features P2/P2′ and P3/P3′ and indicate the cathodic and anodic stability limit of the commensurate c($\sqrt{2}\times2\sqrt{2}$) adlayer structure (region III). We also notice the hysteresis of the scattering intensity when
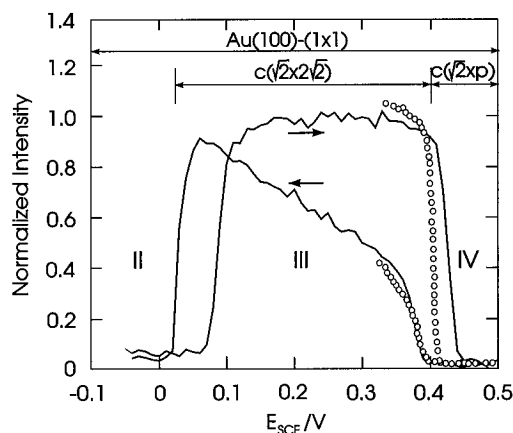

Figure 8. Potential dependence of the normalized scattering intensity at (1,0,0.1) for Au(100)/0.05 M NaBr. Two different scan rates, 1 mV s⁻¹ (—) and 0.2 mV s⁻¹ (○), are shown. The direction of the potential ramp is indicated by arrows. The morphology of all curves is rather independent of the immersion potential.
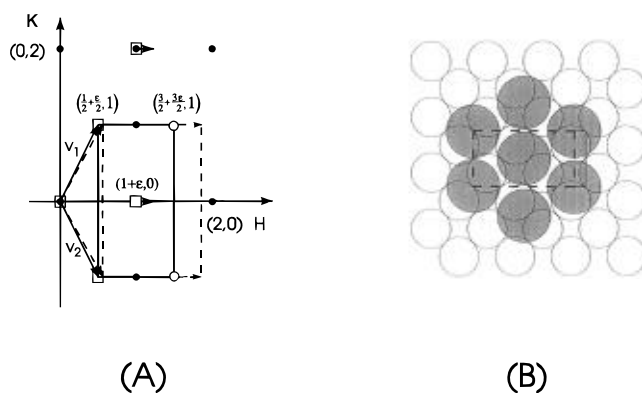

Figure 9. In-plane diffraction pattern (A) and real space representations (B) of the uniaxial commensurate c($\sqrt{2}\times p$)R45° bromide adlayer as obtained for one domain at 0.500 V for Au(100) in 0.5 M NaBr. The shift of the diffraction spots with potential is indicated. Explicitly shown are the unit cells at $E = 0.200$ V (---), e.g., $p = 2\sqrt{2} = 2.828$, and at $E = 0.51$ V (---), with $p = 2.53$. The solid circles represent the substrate surface reflections. The bromide superstructure reflections are indicated by (□); the open circles represent expected superstructure reflections, which were not observed experimentally.

changing the direction of the potential ramp. Kinetic aspects of these phase transitions will be discussed in section 3.3.

Above 0.40 V, which corresponds to the voltammetric feature P3/P3′, the bromide undergoes a commensurate/incommensurate transformation and the diffraction features move continuously and uniaxially outward as shown for one domain in Figure 9A. Despite the changes in the diffraction pattern there is no change in symmetry between the commensurate and the incommensurate phases. In the incommensurate phase reflections are observed for instance at $(1/2 + \epsilon/2,1)$, $(1 + \epsilon,0)$, and $(1/2 + \epsilon/2,-1)$, along with symmetry equivalents. The intensity of the expected higher order reflections, for instance at $(3/2+3\epsilon/2,1)$, $(3/2+3\epsilon/2,-1)$, was too low in order to be detected under the present experimental conditions.

At constant potential all positional changes of the various reflections can be indexed by multiples of the same value of the incommensurability ϵ. The dashed arrows in Figure 9A indicate the potential dependence of the in-plane diffraction pattern in region IV. The incommensurate phase corresponds to a c($\sqrt{2}\times p$)R45° unit cell (Figure 9B) where $p = 2\sqrt{2}/(1 + \epsilon)$. Along the commensurate direction (0,1) the bromide rows are always separated by $\sqrt{2}a_{nn}/2 = 2.04$ Å. The separation along the incommensurate direction (1,0) is given by $\sqrt{2}a_{nn}/(1$

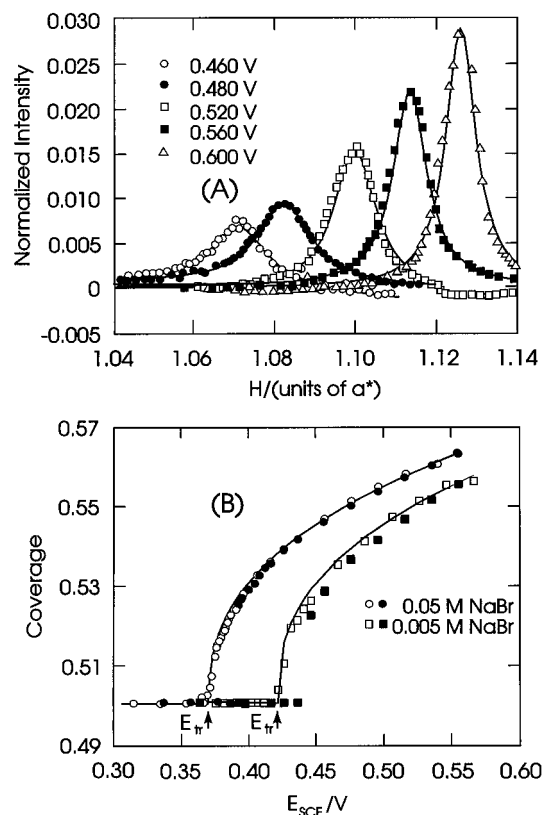**Figure 10.** (A) Diffraction profiles along (H,0,0.1) for Au(100)/0.05 M NaBr at various potentials in region IV. The potential was scanned toward positive values in increments of 5 mV. The solid lines are fits to a Lorenzian line shape. (B) Potential dependence of the bromide adlayer coverage as obtained in the SXS study. The open (filled) symbols represent the negative (positive) going potential scan. The solid lines were calculated with a power law $0.122(E - E_{tr})^{0.39} + 0.5$, where E_{tr} is the concentration-dependent thermodynamically defined transition potential, as indicated in the figure.

$+ \epsilon) = pa_{nn}/2$. This diffraction pattern can be caused by either a uniformly compresssed adlayer or domain walls introduced into the c($\sqrt{2} \times 2\sqrt{2}$) structure. In the latter model the average separation between regions which are locally incommensurate is $a_{nn}\sqrt{2}/\epsilon$. However, the absence of satellite peaks, for instance $(1 - \epsilon, 0)$, at all potentials, is incompatible with a well-ordered superstructure of sharp domain walls (for more detail cf. ref 33). A relatively uniform compression, especially at the largest ϵ, where the bromide densities are close to those found on Au-(111), appears to be the most likely scenario (for more detail cf. ref 33).

In order to measure the potential dependence of the monolayer lattice parameter p, diffraction profiles were acquired along the H direction either at $(1 + \epsilon, 0)$ or at $(1/2, (1 + \epsilon)/2)$ over the available stability region of the c($\sqrt{2} \times p$)R45° in increments of 5–20 mV. Several representative curves measured in the positive scan direction are displayed in Figure 10A. They are well described by Lorenzian line shapes as shown by the solid lines, where $\epsilon(E)$ is obtained from the peak positions. The dimensionless bromide coverage is equal to $\theta = (1 + \epsilon)/2$, which is the ratio of the primitive gold and bromide unit cell areas ($A_{Au} = a_{nn}^2$, $A_{Br} = 2a_{nn}^2/(1 + \epsilon)$). Figure 10B shows the change of the bromide coverage as a function of the applied potential for solutions containing 5 or 50 mM NaBr. The increasing bromide coverage with positive potential corresponds to a uniaxial compression of the rectangular adlayer structure toward a close packed hexagonal arrangement. Furthermore, the concentration dependence of the adlayer coverage at constant

potential indicates a rather completely discharged bromine atom, e.g., the electrosorption valency is close to unity.

A comprehensive account on the specifics of the continuous phase transition c($\sqrt{2} \times 2\sqrt{2}$)R45° $\rightleftarrows$ c($\sqrt{2} \times p$)R45° will be given elsewhere.[33]

3.3. Kinetics of Structural Changes for the System Bromide/Au(100). *3.3.1. General Aspects.* The present SXS study provides detailed information on the structure and stability of the intrinsic gold surface and the two ordered bromide adlayers. On the basis of this knowledge it is now possible to identify the following phase transitions (for guidance we refer to the nomenclature (P1, P2/P2′, P3/P3′) introduced in section 3.1 when describing the cyclic voltammogram): (1) P1 represents the bromide-induced lifting of the Au(100)-(hex) reconstruction. The reverse process is rather slow and does not give rise to a sharp voltammetric feature. (2) The peaks P2/P2′ represent an adlayer disorder/order transition. The ordered structure is commensurate with the substrate. (3) The final adlayer phase transition marked by P3/P3′ is a commensurate to uniaxially incommensurate structural phase transition of the bromide monolayer. Exploring voltammetric experiments with variable scan rates revealed small hysteresis effects for both adlayer transitions. In the following sections we will show that their kinetics can be resolved employing i vs t measurements.

All kinetic measurements have been performed in 0.005 M NaBr/0.045 M NaClO$_4$ in order to reduce bromide migration effects. The morphology of the cyclic voltammogram and of the capacitance vs potential curves (cf. Figures 1 and 2) does not change considerably between 5 and 50 mM NaBr solutions. The only consequence is a small shift of the transition potentials, which are now located at −180 (P1), 40 (P2), 30 (P2′), 422 (P3) and 404 mV (P3′). All three phase transitions are clearly represented in the charge density vs potential curve, which was obtained by integration of the positive going cycle of the corresponding voltammogram, after calibration with 0.05 M NaClO$_4$. Figure 11 also contains the charge balance (see insert) as it is obtained from the quantitative analysis of the current transients (cf. sections 3.3.2. and 3.3.3.).

3.3.2. Stability of the Reconstructed Au(100)-(hex) Phase. Au(100)-(hex) → Au(100)-(1×1). The kinetics of the transition Au(100)-(hex) → Au(100)-(1×1) were previously studied in aqueous acidic solutions containing ClO$_4^-$ and/or SO$_4^{2-}$ ions, e.g. only weakly specifically adsorbed anions, with optical spectroscopy,[7,34] current−time transients,[35] and scanning tunneling microscopy.[30,31] The authors discussed nucleation-and-growth-type mechanisms.

The present electrolyte contains bromide ions, which are strongly specifically adsorbed on the Au(hkl) surface and, in addition, increase significantly the mobility of surface gold atoms.[36] The transient measurements were always started under conditions, where a reconstructed Au(100)-(hex) surface was obtained through flame annealing. The following procedure was applied: The electrode was immersed at $E = -0.500$ V into the aqueous bromide solution and then kept at this potential for 2 min in order to equilibrate. The initial potential of the transient measurement $E_i = -0.230$ V was established through a slow potential scan with 5 mV s^{-1}. After a short holding time of 30 s a single potential step toward various potentials E_f was applied, and the corresponding current was monitored (Figure 12). Double layer charging currents have been minimized by choosing E_i as close as possible to the critical transition potential around P1.

All transients are characterized by an initial exponential-like decay, which is followed by a broad shoulder when the final potentials varied between −0.140 and 0.040 V. In an attempt
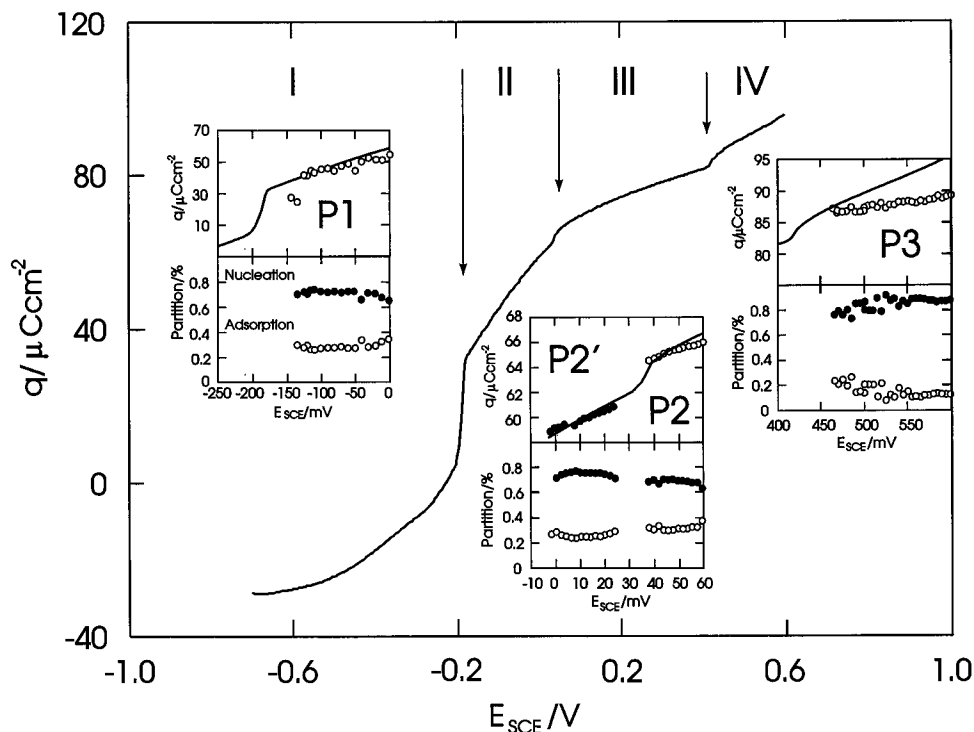
Figure 11. Charge density vs potential plot for Au(100) in 0.005 M NaBr/0.045 M NaClO₄/Au(100) as obtained by integration of a slow positive potential scan of the corresponding cyclic voltammogram with a freshly annealed electrode. The characteristic adlayer regions and the transition potentials are indicated. The insets illustrate the potential dependence of the charge density as obtained with the i vs t step experiments for I → II, II ⇌ III, III ⇌ IV. Each point corresponds to $q_i + (q_{ad} + q_n)$, where q_i is the charge at the initial potential E_i of the respective potential step. The relative contributions of q_n (●) and q_{ad} (○) are plotted in the lower panel of each inset.
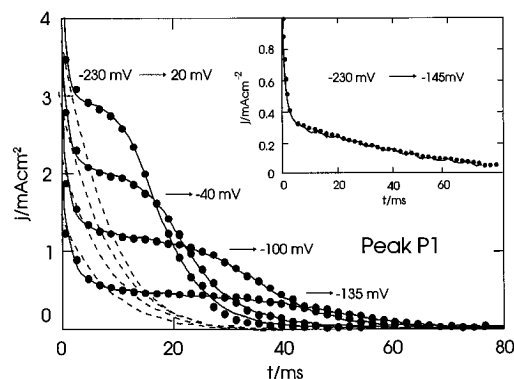

Figure 12. Current transients $i(t)$ for Au(100) in 0.005 M NaBr/0.045 M NaClO₄ obtained with a single potential step from $E_i = -0.230$ V to various final potentials in region II shown as solid lines. Each experiment has been performed with a freshly flame-annealed electrode. The dashed curves correspond to transients measured with the same step regime, but just after the reconstruction has been already lifted once. The dots represent the results of a numerical fit of the experimental data to the adsorption−nucleation model expressed by eq 4. The inset shows one transient measured with $E_i = -0.230$ V/E_f = −0.145 V as a typical example of transitions with low overvoltages, e.g., $E_f < -0.130$ V, with an expanded time scale. The trace represented by the solid dots was calculated with eq 2; see text for further discussion.

to analyze the nature of the transients shown in Figure 12, the following four aspects should be considered:

1. The macroscopic response of the overall process is a charging current (cf. peak P1 in the voltammogram in Figure 1), which reflects the negative shift of the zero charge potential due to the local structural changes of the substrate and due to additional bromide adsorption (cf. section 3.2 and ref 6).

2. The broad shoulder is only observed during the first single potential step, e.g. when starting with a thermally reconstructed, island-free Au(100)-(hex) surface (cf. Figure 5).

3. Only single-exponential transients were measured when

applying the same potential step E_i/E_f a second time, e.g. immediately after the electrochemical lifting of the Au(100)-(hex) reconstruction (dashed curves in Figure 12). Comparing the time scale and the potential step regime of these experiments with the diffractograms plotted in Figure 5 shows that the dashed curves represent exclusively the bromide adsorption on the still unreconstructed Au(100)-(1×1) surface.

4. A recent STM study for Au(100) in 0.01 M H₂SO₄ solution suggested that the formation of the Au(100)-(1×1) domains proceed along the reconstructed Au(100)-(hex) rows via a nucleation process in combination with quasi *one-dimensional* growth at *low overvoltages*.[30]

The above observations provide the foundation for the following model of those $i-t$ transients (I → II), which have been obtained after the first potential step when starting with a freshly flame-annealed reconstructed surface. Immediately after the first potential step E_i/E_f (solid lines in Figure 12) the bromide surface excess increases due to an adsorption-controlled mechanism, which can be expressed by the following equation:[37,38]

$$i_{ad} = k_3 \exp(-k_4 t) \tag{1}$$

where the condition $k_3 = k_4 q_{ad}$ gives the total integrated charge of adsorption as q_{ad}, and k_4 is the adsorption rate constant. An additional current (charge) contribution (i_n) results from subsequent structural changes of the substrate. Considering the result of the *local* STM studies in various electrolyte solutions and at *low overpotentials*,[30] this process is consistent with instantaneous nucleation of the unreconstructed phase at pre-existing defects (steps, domain boundaries), e.g., $N(t) = N_o$, coupled with activation-controlled one-dimensional growth. The geometry of the growing patches does not need to be specified in more detail in this model because expansion is assumed to proceed only in one dimension. Within the framework of the Bewick−Fleischmann−Thirsk theory[39] the corresponding cur-

10284 *J. Phys. Chem., Vol. 100, No. 24, 1996*

Wandlowski et al.

rent can be derived as

$$i_n = k_1 \exp(-k_2 t) \tag{2}$$

where $k_1 = k_2 q_n$, q_n is the total charge of the nucleation-and-growth process, and k_2 is a constant representing the rates of nucleation and growth. Equation 2 can also be interpreted as instantaneous nucleation and two-dimensional growth with surface diffusion control.[40]

The total current is then obtained by adding the two contributions expressed by eq 1 and eq 2:

$$i(t) = k_1 \exp(-k_2 t) + k_3 \exp(-k_4 t) \tag{3}$$

Experimentally we obtained only at low overvoltages (referring to P1), e.g. -0.170 V $< E_f < -0.140$ V, i vs t curves, which can be represented by eq 3 satisfactorily. An example is given in the inset of Figure 12. Subsequent analysis showed that most transients with $E_f > -0.140$ V ($\tau \ll 100$ ms) are better described by

$$i(t) = k_1' t \exp(-k_2 t^2) + k_3 \exp(-k_4 t) \tag{4}$$

with $k_1' = 2k_2 q_n$. The first term in eq 4 accounts for instantaneous nucleation coupled with a two-dimensional growth process.

There exists a small transition region in potential (20–30 mV) between the kinetic mechanisms represented by eqs 3 and 4. Phenomenologically we found that the latter is characterized by exponents of the time variable in the nucleation and growth term changing systematically from $m = 1$ (eq 3) to $m = 2$ (eq 4).

The successful application of eq 4 points to the fact that the strictly one-dimensional law of growth is not adequate at the higher overvoltages. We suggest that the growth process follows a *two-dimensional* activation-controlled mechanism. The fit of our experimental transients with respect to the model expressed by eq 4 gives rather systematic and nearly linear changes of the logarithm of the rate parameters k_1', k_2, k_3, and k_4, which are displayed in Figure 15A, with potential. The standard deviation of the individual constant k_i is usually less than 2% and shows no systematic changes. The quotient $k_1'/k_2 = (65 \pm 3)$ μC cm^{-2} is practically constant within the potential range studied, which indicates a potential independent charge contribution q_n of the nucleation-and-growth process. As shown in the left inset to Figure 11, the ratio q_n:q_{ad} amounts to approximately 0.7:0.3. Only at $E > -50$ mV does the adsorption charge increase slightly due to the increase of the bromide surface excess in region II (Figure 11, Figure 15). Additional support for the model is given by the fact that the charge balance $q_n + q_{ad}$ coincides exactly with the voltammetric results. This is demonstrated in the inset of Figure 11, where the circles correspond to $q_i + (q_{ad}+q_n)$ with q_i as the charge of the initial potential E_i of the respective potential step, and the lines represent the charge densities as obtained from the cyclic voltammetry.

We also notice that all transients monitored when applying the same potential step E_i/E_f a second time, e.g. immedeately after the reconstrtuction has been lifted once, could be satisfactorily modeled with a simple adsorption-controlled mechanism as given by eq 1.

In order to rationalize our observations, the following mechanism is suggested. The lifting of the Au(100)-(hex) reconstruction is initialized by the local specific adsorption of bromide at defect sites (steps, grain boundaries, and domain boundaries of the reconstruction). These sites eventually transform into active nucleation sites which are associated with the lifting of the reconstruction. As a result, the one-dimensional growth of the new phase proceeds along the reconstruction rows and it should be the preferred mechanism. Increasing the bromide coverage with increasing positive potential ($E_f \geq -0.130$ V, Figure 1B) causes practically the instantaneous adsorption of the halide ions not only on preexisting defects, but also on terraces. New nucleation centers will be created within the reconstruction domains due to the limited number of defect sites. The electrosorption of bromide is accompanied by a significant partial charge transfer (Figure 3 and ref 14). The latter could also weaken the gold−gold bonding[41] and therefore facilitate the x−y motion of gold atoms. As a result, the growth process, which is involved in the lifting of the reconstruction, is no longer strictly one-dimensional. This view is supported by the dynamics of "surface grooming" effects reported by Gao et al. for the system Au(100)-[(hex)⇌(1×1)]/I$^-$.[20]

3.3.3. 2D Phase Transitions in Bromide Adlayers on Au-(100)-(1×1). Disordered Adlayer ⇌ c($\sqrt{2} \times 2\sqrt{2}$)R45° (II ⇌ III). The results of our SXS study showed that the formation of the commensurate bromide phase c($\sqrt{2}\times2\sqrt{2}$)R45° in region III is preceded by a fluidlike adlayer in region II. The corresponding charge density vs potential curve, as for instance plotted in Figure 11, exhibits a discontinuity in charge of $\Delta q_1 = 3.0$ μC cm^{-2} around the transition region at P2/P2′. Furthermore, we observed in the voltammetric experiments a small hysteresis when reversing the direction of the potential scan (cf. Figure 1A). These experimental findings indicate that current−time measurements might help to understand the kinetic mechanisms of the transitions.

Typical i vs t curves of the formation of the commensurate structure, obtained after a single potential step with $E_i = 20$ mV (waiting time in region II, 2 min) and various final potentials, are plotted in Figure 13A as solid lines. Effects due to pure double layer charging have been minimized by choosing E_i as close as possible to the transition potential around P2, e.g., within 10 mV. The experimental transients are characterized by an initial exponential-like decay superimposed by a broad plateau (shallow maximum) and finally a steeper region. The former shifts toward shorter times with increasing overvoltage and develops successively into a shoulder. This morphology is rather typical for adsorption coupled with nucleation-and-growth processes.[42] We also note that the initial decay is less steep than that for the transition around P1 (Figure 12) and P3 (Figure 14), which both involve significantly larger charges but the same ionic strength of the bulk electrolyte. Therefore we associate the initial segment of the transient primarily with the oxidative adsorption of additional bromide ions and not with pure double layer charging or electronic hardware response.

It is well-known that defects, such as monatomic high steps, kink sites, and holes, may act as preferred adsorption sites.[43] We now assume that the adsorption at defect sites could provide a reaction path which runs in parallel with a nucleation-and-growth type of phase formation, implying that adsorption and nucleation take place at different surface spots.[44] This general model was tested employing the following diagnostic equation:[45,46]

$$i = k_1'' mt^{m-1} \exp(-k_2 t^m) + k_3 \exp(-k_4 t) \tag{5}$$

The first term in eq 5 represents the general current expression of a nucleation and growth process within the framework of the Bewick−Fleischmann−Thirsk theory;[43,49] m is a parameter which is associated with the dimensionality of nucleation and
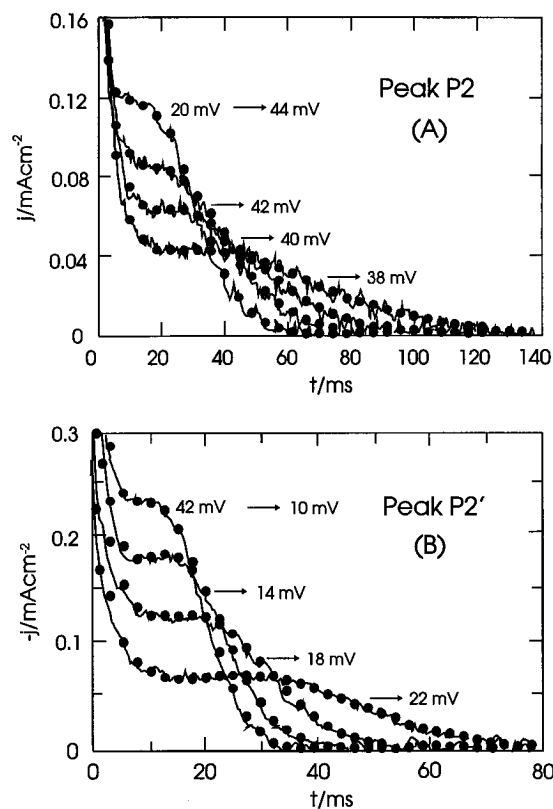
Figure 13. Current transients, shown as solid lines, of the formation (A) and dissolution (B) of the commensurate bromide adlayer c($\sqrt{2}\times2\sqrt{2}$)R45°. The potential steps are indicated in the figure. The solid dots represent the numerical fits of the experimental curves calculated according to the adsorption–nucleation (A) or desorption–hole–nucleation model (B), eq 4.

Figure 14. Current transients of the formation (A) and dissolution (B) of the c($\sqrt{2}\times p$)R45° from the c($\sqrt{2}\times2\sqrt{2}$)R45° bromide adlayer on Au(100). The solid circles represent the numerical fits with respect to eq 7.

of growth, and $k'' = k_2 q_n$. We note that with $m = 2$ or $m = 3$ the well-known equations for instantaneous or progressive nucleation can be obtained, provided that we assume a two-dimensional growth with a constant rate. The second term in eq 5 approximates the adsorption current with a Langmuir-type mechanism.

The analysis of the experimental curves in terms of eq 5 shows agreement between the general model and the transient data. In addition, the data are best described when $m = 2$. This result reduces the number of adjustable parameters necessary to describe the overall kinetic mechanism for the formation of the c($\sqrt{2}\times2\sqrt{2}$)R45° bromide adlayer. Equation 5 simplifies in this case with $k_1' = 2k_2''$ and $m = 2$ to the formalism already given as eq 4 in paragraph 3.3.2. The refined model (shown as filled circles in Figure 13A) represents an excellent description of the experimental i vs t traces (solid lines in Figure 13A) and supports this approach. The potential dependence of the individual constants k_1', k_2, k_3, and k_4 (their standard deviation is less than 3%) is plotted in Figure 15B; log k_1' and log k_2 do not change linearly with potential. Therefore no Butler–Volmer type of potential dependence, as has been assumed for metal UPD processes,[44] is applicable in the present situation. The system resembles more closely the nonlinear characteristics observed for phase formation reactions of neutral species at metal/electrolyte interfaces.[47] This result stresses the fact that the adlayer transition around P2 involves mostly bromine atoms rather than ionic species, which is also suggested by the potential dependence of the transition potentials P2/P2′ (Figure 3). The overall charge $q = q_n + q_{ad}$ is slightly increasing with potential (plotted in Figure 11). The average ratio $q_n{:}q_{ad}$ amounts to 0.69: 0.31 and q_n is very close to the voltammetric value of 3 μC cm⁻², which was obtained at P2. This charge balance demon-
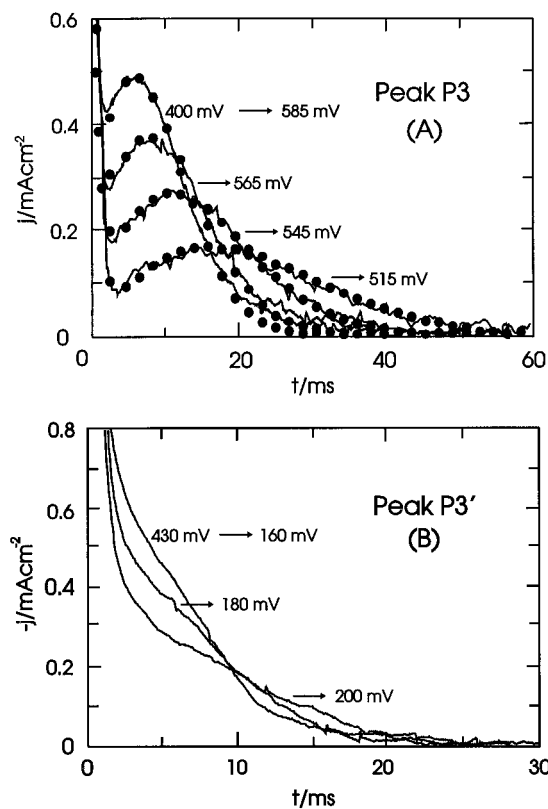
strates the consistency of our thermodynamic data as well as of the proposed kinetic model.

The kinetic data as well as the structural results described in section 3.2 support the following scenario for the transition between the fluidlike disordered bromide phase II and the commensurate structure c($\sqrt{2}\times2\sqrt{2}$)R45° in region III: The initial potential of the transient experiments plotted in Figure 13A was chosen to be close to P2, where $\theta \rightarrow 0.5$. The potential step into the thermodynamic stability region of phase III triggers the "supersaturation" of the fluidlike bromide adlayer. The high coverage and the high mobility of the bromide as well as of the gold atoms in region II cause the instantaneous formation of statistically distributed commensurate nuclei of the c($\sqrt{2}\times2\sqrt{2}$)R45° phase over entire terraces. Edges of the newly formed adlayer islands (growth of the commensurate phase) as well as the still existing step edges of the gold surface will act as sinks for additional adatoms. The high surface mobility of the individual bromine atoms will (a) reduce the probability for the nucleation of additional islands and (b) favor growth controlled by the rate of incorporation into the growing cluster. As a consequence, the adsorption at substrate defects (most probably only step edges) proceeds in parallel with instantaneous nucleation and two-dimensional activation-controlled growth, which might be one physical justification for the application of eq 4.

We have also fitted eq 4 to the i–t curves of the transition c($\sqrt{2}\times2\sqrt{2}$)R45° → disordered adlayer. As shown in Figure 13B, there is good agreement between the data and the model. This suggests that the reductive dissolution of the commensurate bromide adlayer can be described by a combined desorption (most probably at substrate step edges) and a hole-nucleation and two-dimensional growth process, which eventually starts at domain boundaries of the ordered adlayer. The charge
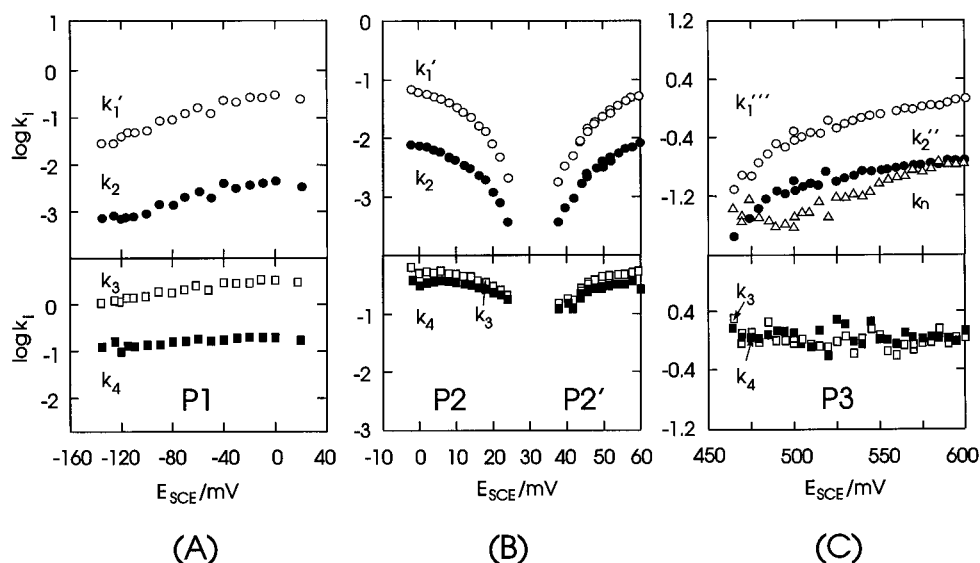
Figure 15. Potential dependence of the constants k_1' (k_1'''), k_2 (k_2''), k_3, k_4, and k_n for the transition regions around P1 ((A), Figure 11) and P2/P2' ((B), Figure 13). The fitted parameters of the transition III → IV, e.g., P3 (Figure 15), are given in (C).

balance and the potential dependence of the individual parameters k_1' to k_4 are plotted in Figure 11 and Figure 15B.

$c(\sqrt{2}\times2\sqrt{2})R45° \rightleftharpoons c(\sqrt{2}\times p)R45°$. The in-plane diffraction experiments revealed that the bromide monolayer undergoes a transition to a uniaxial incommensurate $c(\sqrt{2}\times p)R45°$ monolayer where p continuously decreases from $2\sqrt{2}$ with increasing potential. The data support an atomic model with uniform compression rather than sharp, well-ordered domain walls.[33] The coverage changes continously with potential, but shows a nonnegligible hysteresis when changing the sweep direction, even at effective sweep rates as low as 0.01 mV s^{-1}. The corresponding transients (III → IV) show a well-developed current maximum i_{max} at t_{max} (Figure 14). The maximum shifts to shorter times with increasing overvoltage, e.g. more positive values of E_f. All transients merge for $t \rightarrow \infty$. The overall charge, which can be obtained by current integration, increases monotonously with E_f. The shape of the transients indicates unambiguously the presence of a nucleation and growth process. The initial decay is exponential. Due to its short time scale ($\tau < 3$ ms), it is complicated to distinguish between pure double layer charging and adsorption/reaction control. Formally, both short-time processes can be modeled by an expression identical to eq 1. The reduced variable plot of the long-time response using the measured quantities (i/i_{max}) and (t/t_{max}) showed significant deviations from the response for the limiting cases of one-step progressive or instantaneous nucleation and activation-controlled growth. Consequently we tested the more general diagnostic model expressed by eq 5. Agreement between the experimental transients and eq 5 was found in a systematic test of all data with m ranging between 1.5 and 1.7 as shown in Figure 14A. Noninteger values of m point to the exponential law of nucleation:[47,48]

$$N = N_0 \left(1 - \exp(-k_n t)\right) \quad (6)$$

where N is the number of nuclei, N_o is the maximum possible number of nuclei in the absence of subsequent growth processes, and k_n is the rate of nucleation.

The combination of eq 6 with an appropriate law of growth and taking into consideration the overlapping of growing centers leads to two possibilities, which rationalize Avrami exponents m ranging between 1 and 2. The growth process can be either considered as one-dimensional or, secondly, as controlled by surface diffusion of adions.[46] Applications of the Bewick—

Fleischmann−Thirsk approach[39] yields

$$i = k_1'''(1 - \exp(-k_n t)) \exp(-k_2''(t - (1/k_n) \times$$
$$(1 - \exp(-k_n t)))) + k_3 \exp(-k_4 t) \quad (7)$$

$k_1''' = k_n q_n$, k_n is the nucleation rate and k_2'' is a constant, which is directly related to the nature of the growth mechanism.

Figure 14 illustrates the agreement between the experimental transients of the formation of the bromide adlayer $c(\sqrt{2}\times p)$-R45° and those calculated with eq 7. The potential dependence of the individual parameters is plotted in Figure 15C. The adsorption rate k_4 and the charge $q_{ad} = k_3/k_4$ are practically constant over the entire 150 mV potential range studied. This observation is related to the minor change of the adsorbate coverage with potential in region IV ($0.5 < \theta < 0.56$; cf. Figure 10B). The nucleation charge is monotonously increasing with E_f due to the continuous compression of the $c(\sqrt{2}\times p)R45°$ adlayer. The extra bromide ions (bromine atoms) are probably incorporated into the lattice at step edges or at domain boundaries on terraces. The initial configuration in III is $c(\sqrt{2}\times2\sqrt{2})R45°$, e.g., $p = 2\sqrt{2}$. The compression is unidirectional, as obtained from the X-ray diffraction studies, and provides a supportive argument for an activation-controlled, but one-dimensional growth mechanism. On the other hand it is also plausible to rationalize surface diffusion controlled growth by assuming that the process of reorganizing the stable substrate−adsorbate superpositions is slow, after the incorporation of additional bromide ions, because most adlayer species have to move out of their energetically rather favorable bridge positions. The unambiguous answer is not yet possible at this stage because we did not succeed in measuring meaningful and clearcut purely growth-controlled transients in double-step experiments.

The dissolution of the uniaxial commensurate phase $c(\sqrt{2}\times p)$-R45° (P3', IV → III) is characterized by monotonous i vs t curves (Figure 14B). Their physical nature is associated with an expansion of the $c(\sqrt{2}\times p)R45°$ layer up to $p = 2\sqrt{2}$.

4. Summary and Conclusions

The adsorption and phase formation of bromide ions on Au-(100) has been studied with in-situ surface X-ray diffraction and i vs t transient measurements. The presence of small bromide surface excess at the Au(100)-(hex) surface causes the

Structural and Kinetic Aspects of Br⁻ Adsorption on Au(100)

J. Phys. Chem., Vol. 100, No. 24, 1996 **10287**

abrupt lifting of the substrate reconstruction. No ordering of the adlayer is required or involved. The corresponding charge density just before the onset of the transition ranges between -2 and $-8\mu C\ cm^{-2}$, which is close to E_{pzc}. The lifting of the substrate reconstruction proceeds at high overpotentials via instantaneous nucleation and two-dimensional growth. It is noteworthy to mention that the growth mechanism seems to change at low overpotentials toward a one-dimensional or surface diffusion controlled process.

Two ordered bromide adlayer phases were found on the unreconstructed Au(100)-(1×1) surface: a commensurate $c(\sqrt{2}\times2\sqrt{2})R45°$ phase and at more positive potentials a uniaxial incommensurate $c(\sqrt{2}\times p)R45°$ phase. The disorder/order transition, which refers to the formation and dissolution of the commensurate phase, proceeds via instantaneous island (hole) nucleation and activation-controlled growth in combination with a parallel adsorption (desorption) process at substrate surface defects.

The formation of the slightly more dense $c(\sqrt{2}\times p)R45°$ adlayer can be described by the exponential law of nucleation in combination with either one-dimensional activation-controlled or surface diffusion controlled growth. Both growth regimes could not be clearly distinguished via transient studies or structural arguments.

Our investigations allowed a rather detailed assignment of all voltammetric features of the bromide adsorption on Au(100) to the respective structural properties, their stability, and their transition kinetics. Further comparative studies with other halides and coadsorbed systems will illuminate the substrate- and adsorbate-specific aspects of two-dimensional phase transitions in anionic and saltlike adlayers on single-crystalline electrodes.

References and Notes

(1) Farell, H. H. In *The Chemical Physics of Solid Surfaces and Heterogeneous Catalysis*; King, D. A., Eds.; Woodruff, D. P. Elsevier: New York, 1987; Vol. 36, p 225.

(2) Dowden, P. A. *Crit. Rev. Solid State Mat. Sci.* **1987**, *13*, 191.

(3) Hamelin, A. *J. Electroanal. Chem.* **1982**, *142*, 299.

(4) Hamelin, A. *J. Electroanal. Chem.* **1983**, *144*, 365.

(5) Hamelin, A.; Vitanov, T.; Sevastjanov, E.; Popov, A. *J. Electroanal. Chem.* **1983**, *145*, 225.

(6) Kolb, D. M.; Schneider, D. *Electrochim. Acta* **1986**, *31*, 929.

(7) Friedrich, A.; Shannon, C.; Pettinger, B. *Surf. Sci.* **1991**, *251/252*, 587.

(8) Ocko, B. M.; Wang, J. In *Proceedings of the Workshop on Structural Effects in Electrocatalysis and Oxygen Electrochemistry*; Scherson, D., Tryk, D., Daroux, M., Xing, X., Eds.; Electrochem. Soc.: Pennington 1992; p 147.

(9) Wang, J.; Ocko, B. M.; Davenport, A. J.; Isaacs, H. S. *Phys. Rev.* **1992**, *B46*, 10321.

(10) Ocko, B. M.; Magnussen, O. M.; Adzic, R. R.; Wang, J. X.; Shi, Z.; Lipkowski, J. *J. Electroanal. Chem.* **1994**, *376*, 35.

(11) Kolb, D. M.; Lehmpfuhl, G.; Zei, M. S. *J. Electroanal. Chem.* **1984**, *179*, 289.

(12) Zei, M. S.; Lehmpfuhl, G.; Kolb, D. M. *Surf. Sci.* **1986**, *221*, 23.

(13) Kolb, D. M. *Z. Phys. Chem. NF* **1987**, *154*, 179.

(14) Van Huong, C. N.; Hinnen, C.; Rousseau, A. *J. Electroanal. Chem.* **1983**, *151*, 149.

(15) Shi, Z.; Wu, S.; Lipkowski, J. *Electrochim. Acta* **1995**, *40*, 3.

(16) Deakin, M. R.; Li, T. T.; Melroy, O. R. *J. Electroanal. Chem.* **1988**, *243*, 343.

(17) Wiechers, J.; Twomey, T.; Kolb, D. M.; Behm, R. J. *J. Electroanal. Chem.* **1988**, *248*, 460.

(18) Kolb, D. M.; Dakkouri, A. S.; Batina, N. In *Nanoscale Probes of Solid/Liquid Interfaces*; Gewirth, A. A., Siegenthaler, H., Eds.; NATO ASI Series E 288; Kluwer: Dordrecht, 1995; p 263.

(19) Gao, X.; Weaver, M. *J. Am. Chem. Soc.* **1992**, *114*, 8544; *J. Phys. Chem.* **1993**, *97*, 8685.

(20) Gao, X.; Edens, G. J.; Liu, F.; Hamelin, A.; Weaver, M. J. *J. Phys. Chem.* **1994**, *98*, 8086.

(21) Gao, X.; Edens, G. J.; Weaver, M. J. *J. Phys. Chem.* **1994**, *98*, 8074.

(22) Ocko, B. M.; Watson, G. M.; Wang, J. X. *J. Phys. Chem.* **1994**, *98*, 897.

(23) Tao, N. J.; Lindsay, S. M. *J. Phys. Chem.* **1992**, *96*, 5213.

(24) Magnussen, O. M.; Ocko, B. M.; Adzic, R. R.; Wang, J. X. *Phys. Rev.* **1995**, *B51*, 5510. Magnussen, O. M.; Wang, J. X.; Adzic, R. R.; Ocko, B. M. *J. Phys. Chem.*, submitted for publication.

(25) Dickertmann, D.; Koppitz, F. D.; Schultze, J. W. *Electrochim. Acta* **1976**, *21*, 967.

(26) Magnussen, O. M.; Hageböck, J.; Hotlos, J.; Behm, R. J. *Faraday Discuss. Chem. Soc.* **1992**, *94*, 329.

(27) Scherson, D. A.; Kolb, D. M. *J. Electroanal. Chem.* **1984**, *176*, 353.

(28) Hölzle, M.; Wandlowski, Th.; Kolb, D. M. *J. Electroanal. Chem.* **1995**, *394*, 271.

(29) Ocko, B. M.; Wang, J. X.; Davenport, A.; Isaacs, H. *Phys. Rev. Lett.* **1990**, *65*, 1466.

(30) Magnussen, O. M.; Hotlos, J.; Behm, R. J.; Batina, N.; Kolb, D. M. *Surf. Sci.* **1993**, *296*, 310.

(31) Gao, X.; Edens, G. J.; Hamelin, A.; Weaver, M. J. *Surf. Sci.* **1993**, *296*, 333.

(32) Bertel, E; Netzer, E. P. *Surf. Sci.* **1980**, 97, 409.

(33) Ocko, B. M.; Wang, J. X.; Magnussen, O. M.; Wandlowski, Th. *Physica B*, in press; Ocko, B. M.; Magnussen, O. M.; Wang, J. X.; Wandlowski, Th. *Phys. Rev. B Rapid Commun.* **1996**, *53*, R7654.

(34) Kolb, D. M.; Schneider, J. *Surf. Sci.* **1985**, *162*, 765. Schneider, J.; Kolb, D. M. *Surf. Sci.* **1988**, *193*, 579.

(35) Skoluda, P.; Kolb, D. M. *Surf. Sci.* **1992**, *260*, 229.

(36) Alonso, C.; Salvarezza, R. C.; Vara, J. M.; Arvia, A. J. *Electrochim. Acta.* **1990**, *35*,1331.

(37) Lorenz, W.; Möckel, F. *Z. Elektrochem.* **1956**, *60*, 939.

(38) Barradas, R. G.; Bosco, E. *J. Electroanal. Chem.* **1985**, *193*, 23.

(39) Fleischmann, M.; Thirsk, H. R. In *Advances in Electrochem. and Electrochemical Engineering*; Delahay, P., Tobias, C., Eds.; Interscience: New York, 1963; Vol. 3, p 1. Bewick, A.; Fleischmann, M.; Thirsk, H. R. *Trans. Faraday Soc.* **1962**, *58*, 2200.

(40) Armstrong, R. D.; Harrison, J. A. *J. Electrochem. Soc.* **1969**, *116*, 328.

(41) Sette, F.; Hashizume, T.; Comin, F.; MacDowell, A. A.; Citrin, R. H. *Phys. Rev. Lett.* **1988**, *61*, 1384.

(42) Bosco, E.; Rangarajan, S. *J. Chem. Soc., Faraday Trans.* **1981**, *77*, 1673.

(43) Ganon, J.; Clavilier, J. *Surf. Sci.* **1984**, *145*, 487.

(44) Hölzle, M.; Retter, U.; Kolb, D. M. *J. Electroanal. Chem.* **1994**, *371*, 101.

(45) Wandlowski, Th.; Lampner, D.; Lindsay, S. M. *J. Electroanal. Chem.*, in press.

(46) *Instrumental Methods in Electrochemistry*; Southampton Electrochemical Group; Ellis Horwood: New York, 1990.

(47) Buess-Herman, C. *Prog. Surf. Sci.* **1994**, *46*, 335.

(48) Abyaneh, M. Y.; Fleischmann, M. *Electrochim. Acta* **1982**, *27*, 1513.